The rock abrasion record at Gale Crater: Mars Science Laboratory results from Bradbury Landing to Rocknest

N. T. Bridges[1], F. J. Calef[2], B. Hallet[3], K. E. Herkenhoff[4], N. L. Lanza[5], S. Le Mouélic[6], C. E. Newman[7], D. L. Blaney[2], M. A. de Pablo[8], G. A. Kocurek[9], Y. Langevin[10], K. W. Lewis[11], N. Mangold[6], S. Maurice[12], P.-Y. Meslin[12], P. Pinet[12], N. O. Renno[13], M. S. Rice[14], M. E. Richardson[7], V. Sautter[15], R. S. Sletten[3], R. C. Wiens[6], and R. A. Yingst[16]

[1]Applied Physics Laboratory, Laurel, Maryland, USA, [2]Jet Propulsion Laboratory, Pasadena, California, USA, [3]Department of Earth and Space Sciences, College of the Environments, University of Washington, Seattle, Washington, USA, [4]U.S. Geological Survey, Flagstaff, Arizona, USA, [5]Los Alamos National Laboratory, Los Alamos, New Mexico, USA, [6]LPGNantes, UMR 6112, CNRS/Université de Nantes, Nantes, France, [7]Ashima Research, Pasadena, California, USA, [8]Universidad de Alcala, Madrid, Spain, [9]Department of Geological Sciences, Jackson School of Geosciences, University of Texas at Austin, Austin, Texas, USA, [10]Institute d'Astrophysique Spatiale, Université Paris-Sud, Orsay, France, [11]Department of Geosciences, Princeton University, Princeton, New Jersey, USA, [12]Centre National de la Recherche Scientifique, Institut de Recherche en Astrophysique et Planétologie, CNRS-Université Toulouse, Toulouse, France, [13]Department of Atmospheric, Oceanic, and Space Science; College of Engineering, University of Michigan, Ann Arbor, Michigan, USA, [14]Division of Geological and Planetary Sciences, California Institute of Technology, Pasadena, California, USA, [15]Lab Mineral and Cosmochim Museum, Paris, France, [16]Planetary Science Institute, Tucson, Arizona, USA

Abstract Ventifacts, rocks abraded by wind-borne particles, are found in Gale Crater, Mars. In the eastward drive from "Bradbury Landing" to "Rocknest," they account for about half of the float and outcrop seen by Curiosity's cameras. Many are faceted and exhibit abrasion textures found at a range of scales, from submillimeter lineations to centimeter-scale facets, scallops, flutes, and grooves. The drive path geometry in the first 100 sols of the mission emphasized the identification of abrasion facets and textures formed by westerly flow. This upwind direction is inconsistent with predictions based on models and the orientation of regional dunes, suggesting that these ventifact features formed from very rare high-speed winds. The absence of active sand and evidence for deflation in the area indicates that most of the ventifacts are fossil features experiencing little abrasion today.

1. Introduction

Mars is a dry planet, with actively blowing sand in many regions [*Silvestro et al.*, 2010; *Chojnacki et al.*, 2011; *Hansen et al.*, 2012; *Bridges et al.*, 2012a, 2012b]. In the absence of stable liquid water and an active hydrosphere, rates of chemical weathering are slow, such that aeolian abrasion is a dominant agent of landscape modification where sand is present and winds above threshold occur at sufficient frequency. In areas of active sand migration, abrasion rates are estimated at $\sim$1–50 μm yr^{-1} [*Bridges et al.*, 2012b]. Reflecting this activity, ventifacts, rocks that have been abraded by wind-borne particles, are common on the Martian surface. They were tentatively identified in Viking Lander pictures [*McCauley et al.*, 1979] and unequivocally from the much clearer and closer (because of rover mobility) Pathfinder [*Bridges et al.*, 1999] and later Mars Exploration Rover images [*Sullivan et al.*, 2005; *Greeley et al.*, 2006, 2008; *Thomson et al.*, 2008]. They provide invaluable markers of the Martian wind record and insight into climate and landscape modification. Of the seven locations so far visited by landed spacecraft, Gale Crater is probably the best for understanding wind effects on Mars. With active sand dunes [*Silvestro et al.*, 2012] and a central mound whose formation, erosion, and likely exhumation has been heavily driven by aeolian processes [*Malin and Edgett*, 2000; *Anderson and Bell*, 2010; *Milliken et al.*, 2010; *Thomson et al.*, 2011; *Kite et al.*, 2013], wind has been and remains a major geologic agent. The study of ventifacts in Gale therefore provides insight into these fundamental issues.

Terrestrial research shows that ventifacts can be identified by diagnostic shape and textural attributes at the macroscale and microscale [*Laity and Bridges*, 2009]. The shapes are characterized by one or more facets, separated by sharp keels that form through progressive planation. A facet is a relatively planar surface cut by

the wind, regardless of the original rock shape, and a keel is the prominent boundary between two facets. In-profile facet angles relative to the surface vary from nearly vertical to subhorizontal, although commonly are at intermediate angles of 20–60°, depending on rock hardness (marble, ~20–30°; granite, ~40–50°; and basalt, ~50–60°), below which abrasion efficiency declines [*Laity and Bridges*, 2009]. Multiple facets may develop, related not only to changing wind directions but also to the shifting and overturning of small ventifacts. Some facets abut at their lower terminus against a sill at the rock base that is oriented approximately vertical in profile [*Sharp*, 1964; *Bridges et al.*, 2004; *Laity*, 2009]. These form because basal portions of a rock are subjected to less intense abrasion, being lower in the kinetic energy flux profile that peaks several tens of centimeters above the surface [*Anderson*, 1986], within the shadow zone of adjacent rocks, or protected by soil that is subsequently deflated. Elongated pits, scallops and flutes, and grooves constitute the main macroscale (~centimeters) textures and form on windward faces oriented nearly orthogonal, inclined, and subparallel, respectively, to the formative sand-laden winds [*Maxson*, 1940; *Sharp*, 1949; *Smith*, 1984; *Laity*, 1987, 1994; *Bishop and Mildenhall*, 1994; *Laity and Bridges*, 2009, 2013]. These textures commonly transition from one to another, and various papers have used overlapping, and sometimes even contradictory, definitions. Here we use the nomenclature as defined in *Laity and Bridges* [2013]. Scallops, sometimes referred to as crescents, are shallow and u-shaped. Flutes are indentations that are semicircular in cross section and elliptical in plan view. Grooves are similar to flutes but extend across most or all of a face, generally on the upper and top sides where sand flow is nearly parallel to the rock. At the submillimeter microscale, lineations are found, some within macroscale textures.

The ability for rocks to develop prominent ventifact textures is dependent on differences in abrasion resistance, which itself is a function of strength, density, and primary texture [*Laity and Bridges*, 2013]. For example, flutes and fingerlike projections (also referred to as rock tails, fretting, or dedos (Spanish for "finger")) form due to differential abrasion resistance of the component minerals or rock constituents (e.g., conglomerates) [*McCauley et al.*, 1979; *Breed et al.*, 1989; *Lancaster*, 1984; *Laity*, 1994]. Conversely, many basalts, although having an aphanitic mineral distribution that is effectively homogeneous at the scale of impacting sand, contain vesicles and other cavities that present variable geometries and enclosures for multiple sand rebounds such that abrasion is enhanced leading to the development of elongated pits, scallops, flutes, and grooves [*Varkonyi and Laity*, 2012]. Layered rocks with variable hardnesses tend to develop etched surfaces [*Laity*, 2009; *Laity and Bridges*, 2013]. Large boulders and bedrock are the best indicators of regional wind direction, whereas smaller float ventifacts are less reliable because they can be moved by strong wind and water action, animal disturbance, and other geomorphic processes [*Hoare et al.*, 2002; *Laity*, 2009; *Laity and Bridges*, 2013]. In addition, windflow around microtopography close to the ground can deviate from regional trends. In summary, ventifact shape and associated surface features depend on rock size, density and hardness, primary texture, and the amount of abrasion that has occurred.

On Earth, ventifacts develop in vegetation-free areas subject to frequent, high-speed, sand-laden winds, with common environments being deserts, glacial margins, and beaches [*Knight*, 2008]. Unlike aeolian bedforms, wind tails, wind streaks, and other features formed from the accumulation or removal of sediment, ventifacts, being carved out of rock, provide an integrated record of winds above threshold, especially those necessary to propel grains to kinetic energies sufficient to cause abrasion. The dip direction of facets and the orientation of the long axis of elongated pits, scallops, flutes, and grooves are tied to the direction of high-speed winds [*Blackwelder*, 1929; *Sharp*, 1964; *McKenna-Neumann and Gilbert*, 1986; *Bridges and Laity*, 2013]. In most cases wind polarity (e.g., 90° versus 270°) can be determined by the dip direction of facets, the location of abrasion textures on such facets and slopes, and the position of open and enclosed boundaries of scallops and flutes, which are generally (although not always) located on the downwind and upwind ends, respectively. Many ventifacts on Earth exhibit two and sometimes three or more facets or textural imprints, with one direction generally dominant over the others, indicating differences in the integrated energy of sand-laden winds. Ventifacts have therefore been used to map paleowind directions [*Laity*, 1987].

The geochemistry of ventifacts is like that of unabraded rocks unless coatings or rinds are being removed or deposited by the abrasion process (coatings are exogenous material deposited on the rock, whereas rinds are alteration involving the original outer rock surface). Coatings can include desert varnish [*Potter and Rossman*, 1977, 1979; *Dorn*, 1998] and salts, whereas amorphous silica [*Farr and Adams*, 1984] is a common rind formed through partial reaction with the primary rock. Field evidence shows that fossil ventifacts commonly have rock varnish and lichens [*Bishop and Mildenhall*, 1994; *Wilson et al.*, 2002] and evidence for chemical erosion [*Laity*, 2009]. If rock coatings or rinds are initially present and, integrated over time, their growth exceeds the thickness of material

removed by abrasion, then abraded and nonabraded surfaces may show differences in the abundances of coatings/rind diagnostic elements. In addition, the coatings or rinds may affect the abrasion susceptibility of the surface [*Kraft and Greeley*, 2000]. In contrast, abrasion may also form coatings. Field studies show that some ventifacts have a hard rind with a vitreous sheen that may develop through annealing and densification from repeated sand impacts [*Laity and Bridges*, 2013]. Such "case hardening" has not been thoroughly studied, and whether there are geochemical effects from the process is not known. On Mars, alteration can occur through the reaction of water films with basaltic rocks, soils, and airfall dust, forming a rind rich in mobile elements. Lithium in particular is a trace element that could show enhanced abundance from this reaction, such that the detection of Li on the surface of rocks, with lower abundances in the interior, may be used as an indicator of surface alteration [*Ollila et al.*, 2014]. If such alteration is common on Mars, then a lack of Li abundance differences with depth may suggest that rates of abrasion are greater than those of rind/coating development or that abrasion occurred later.

The Mars Science Laboratory (MSL) "Curiosity" payload is well suited for studying ventifacts and modern wind patterns which are relevant for understanding current abrasion conditions. The rover mast cameras, Navigation Camera (Navcam), Mast Camera (Mastcam), and the Chemistry and Camera (ChemCam) instrument remote microimager (RMI) provide images of varying coverage and spatial scale. Navcam, with a pixel scale of 0.82 mrad, provides monochrome stereo imaging, with partial or complete panoramas taken at most rover stoping points [*Maki et al.*, 2011]. The stereo data are converted to a topographic mesh as a standard product available to the MSL team, allowing measurement of the position (*x*, *y*, and *z*) of points and surface orientations of line fits at distances of up to ~45 m. Mastcam provides stereo color imaging with two cameras, M34 (34 mm focal length) (left eye) and M100 (right eye), with pixel scales of 220 and 74 μrad, respectively [*Malin et al.*, 2010]. RMI, at 19.6 μrad/pixel [*Maurice et al.*, 2012; *Le Mouélic et al.*, 2014], is the highest-resolution remote imager ever put on a planetary surface in terms of pixel sampling, exceeded only in spatial scale by microscopic imagers placed close to rocks and soils. With radiometric processing to correct for nonlinearity and flat field, fine details can be discerned [*Langevin et al.*, 2013; *Le Mouélic et al.*, 2014]. The Mars Hand Lens Imager (MAHLI), located on the rover arm, can get close enough to the surface to yield a spatial resolution as fine as 14.5 μm at a working distance of 22 mm [*Edgett et al.*, 2009]. The Rover Environmental Monitoring Station measures wind speed and direction, pressure, relative humidity, air temperature, ground temperature, and ultraviolet radiation, with 1 Hz sampling for over 5 min every hour and periodic (generally daily) observations for durations of an hour or more [*Gomez-Elvira et al.*, 2011] (The wind data are still undergoing calibration as of this writing and are therefore not reported here but are nevertheless highlighted in anticipation of the information they will provide for future interpretations of the aeolian record.). ChemCam LIBS (laser-induced breakdown spectroscopy) detects the presence of and, through partial least squares modeling against a calibration data set, abundance estimates of major and many minor elements within a spot size less than 0.5 mm [*Maurice et al.*, 2012; *Wiens et al.*, 2012]. Observations may consist of single-analysis points or linear to gridded rastered multipoint sequences, with each point usually comprising 30 or 50 laser shots that progressively penetrate to depths of several tens of microns, depending on the target [*Wiens et al.*, 2012]. The first three to five shots typically sample surface dust. LIBS observations are preceded and followed by RMI images that provide geologic context and identify the locations where the laser sampled. All of these instruments provide unique and necessary information for understanding ventifacts and the history of aeolian abrasion in Gale Crater.

The purpose of this paper is to document ventifacts and other evidence for rock wind abrasion as observed by the MSL payload during Curiosity's traverse from Bradbury Landing to Rocknest in the first 100 sols of the mission and put these observations in a context that helps us understand the geologic history of Gale Crater. We begin with a discussion of the methodologies used, focusing on image compilation and interpretation, Navcam stereo data analysis, mapping, mesoscale wind modeling, and LIBS results regarding surface alteration. This is followed by a distillation of the major results of the study, principally the distribution, multiscale morphology, and orientation of the ventifacts, the magnitude and trends of winds predicted by the models, and possible evidence for surface alteration removal. These data are then compared, providing insight on the formative winds that dominated abrasion in the Bradbury-Rocknest region and implications for overall physical weathering in Gale. We conclude that high-intensity westerly flow has dominated the rock surfaces seen by the rover, which may represent the imprint of very rare, high-energy winds integrated over long timescales or a paleowind direction, with the presence of colocated nonabraded rocks indicating that these have greater abrasion resistance or a lesser exposure age, either through shielding from wake protection or burial or transport from another location.
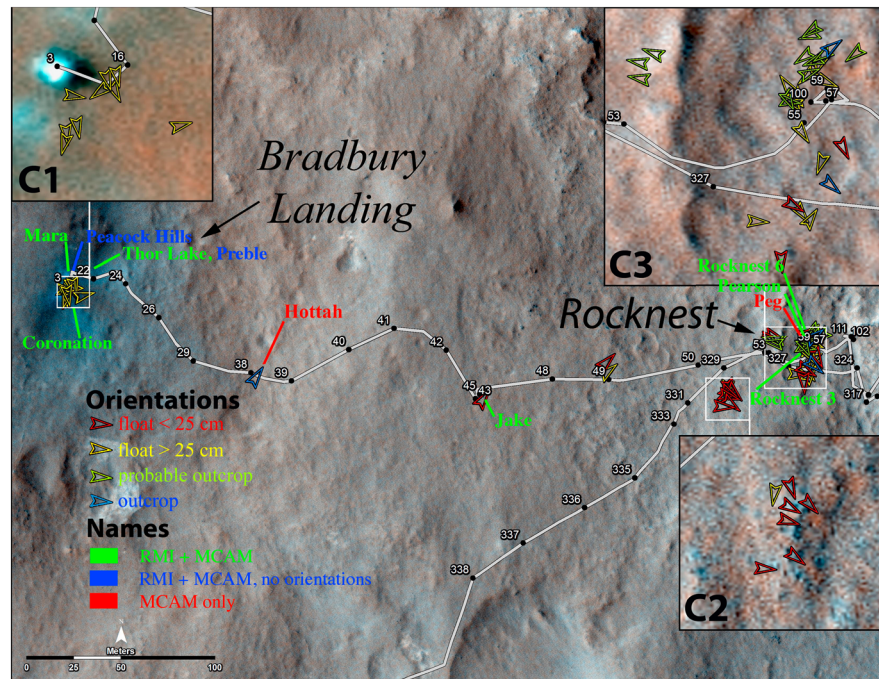
Figure 1. Curiosity's traverse through Sol 338 overlaid on the color portion of HiRISE image PSP_010573_1755. The white numbering shows the rover position as a function of sol. Arrows point toward the inferred downwind direction indicated by ventifact facets and textures, with each arrow representing the mean value for each rock measured through Sol 100 (Table S1). The arrows are color coded to reflect the type of ventifact, as shown in the legend. Three enlargements of ventifact clusters (C1, C2, and C3) are shown. The colored labels are ventifacts for which informal names were given by the MSL science team, with green indicating those that had RMI and Mastcam coverage and red Mastcam only. The rocks Peacock Hills and Preble (blue) were imaged by RMI and Mastcam but were too small to measure orientations in MSLICE using Navcam stereo.

2. Methods

Ventifacts were identified based on the attributes described above in systematic searches through all M100, RMI, and MAHLI images, the three data sets with the highest spatial resolution (Table S1 in the supporting information). M34 and Navcam were also examined in ventifact-rich areas found with the other cameras but not searched systematically because of their lower resolution. Mars Descent Imager data were not used in this study. Diagnostic characteristics were tabulated for each ventifact, including (1) overall shape (facet, keel, and basal sill), (2) macrotexture (elongated pits, scallops, flutes, grooves, and rock tails), and (3) microtexture (lineations). Once found, rocks were located in the lower resolution Navcam data, such that the location, size (height and width), and orientation of most ventifacts could be computed using Navcam stereo mosaics in the Mars Science Laboratory Interface (MSLICE) software package available to the MSL Team [*Aghevli et al.*, 2006; *Crockett et al.*, 2011]. Because of inherent resolution limitations, the orientation of facets and general trends of large textures were determined, with the average taken of three measurements for each rock. In some cases, the topographic mesh did not cover the rocks so that position and orientation could not be measured, and some rocks were too small or far away to measure orientations. These include the rocks Peacock Hills and Preble that were identified as ventifacts in RMI images. For these two rocks, sizes were approximately measured in the RMI images (because the distance to the rocks and therefore pixel scale was known), but orientation of features could not be accurately computed. RMI and MAHLI data were examined to provide qualitative information on microscale abrasion patterns for comparison to the coarser-scale rock textures and shapes seen with Mastcam and Navcam. The Hottah outcrop had a poor Navcam stereo mesh that prevented the retrieval of orientations. Because of the strong desire to measure the prominent rock tails and grooves in Hottah, Jet Propulsion Laboratory (JPL)'s Operations Product Generation Subsystem (OPGS) Group made an orthorectified overhead composite image from Mastcam M100 data from which texture orientation was accurately measured.

The ventifact locations were projected onto the color portion of an orthorectified high-resolution imaging science experiment (HiRISE) image (PSP_010573_1755) with an overlain rover traverse path and sol location
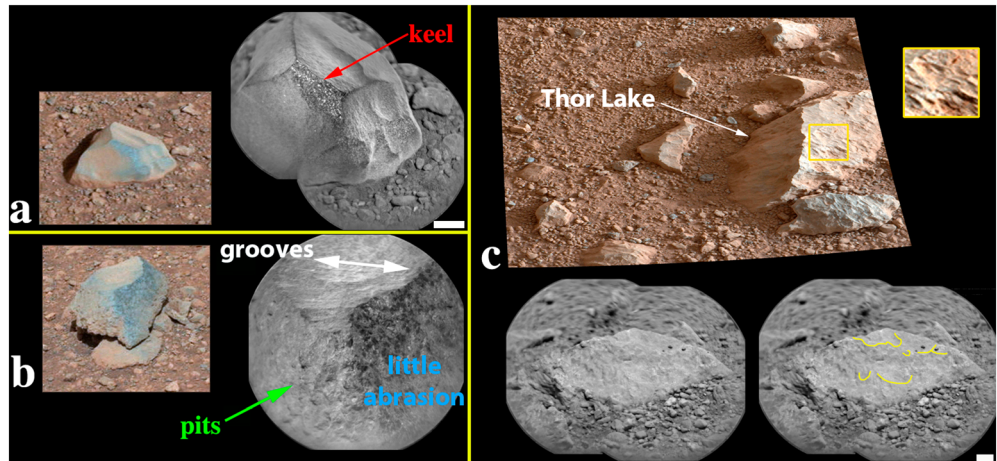
Figure 2. Ventifacts in the Bradbury Landing region (Cluster 1). White bar corresponds to 1 cm in all RMI images. (a) Coronation rock from Mastcam left mosaic mcam00007 (left) and RMI (right). The Mastcam viewing azimuth is 150°. Note prominent facets separated by sharp keels, suggesting multiple wind directions, or, given that this rock is small, rotation since emplacement. (b) Mara rock from Mastcam left mosaic mcam00007 (left) and RMI (right). The Mastcam viewing azimuth is 113°. The RMI image shows that the left edge is dominated by pits and the top by grooves, features likely enhanced by and formed from, respectively, sand abrasion. The right side shows little evidence for abrasion. (c) Thor Lake rock from Mastcam right mosaic mcam00050 (top) and RMI (bottom). The Mastcam viewing azimuth is 107°. Note the scallops on both facets of Thor Lake that are separated by a keel, suggesting two formative wind directions. Nearby rocks are also faceted. An enlargement of the scalloped texture in the Thor Lake Mastcam image is shown at the upper right, with the long axes of the scallops extending from lower right (upwind) to upper left (downwind). In the RMI image, which views Thor Lake from the right relative to the Mastcam perspective, scallops open toward the top of the facet, indicating the downwind direction. Interpretative scallop outlines are shown in yellow in the lower right image. All of these rocks are small, and Mara is perched on another rock, making them unreliable indicators of paleowind directions (see Figure 8).

markers (Figure 1). Each ventifact orientation was plotted with an arrow symbol oriented toward the inferred downwind direction and color coded based on whether the rock was float < 25 cm, float > 25, probable outcrop, or definite outcrop. The orientations were also compiled into rose diagrams and, following past convention [*Laity*, 1994; *Bridges et al.*, 2004], shown as a function of upwind direction (note that some references plot ventifacts in the downwind direction [e.g., *Greeley et al.*, 2008; *Thomson et al.*, 2008], so care must exercised in comparing different data sets).

The MarsWRF (Weather Research and Forecasting) atmospheric model was used to predict the present-day wind field at the MSL landing site and the expected orientation of dunes assuming that they represent the current wind regime. MarsWRF is a global-to-mesoscale model of the Martian atmosphere and is the Mars version of the
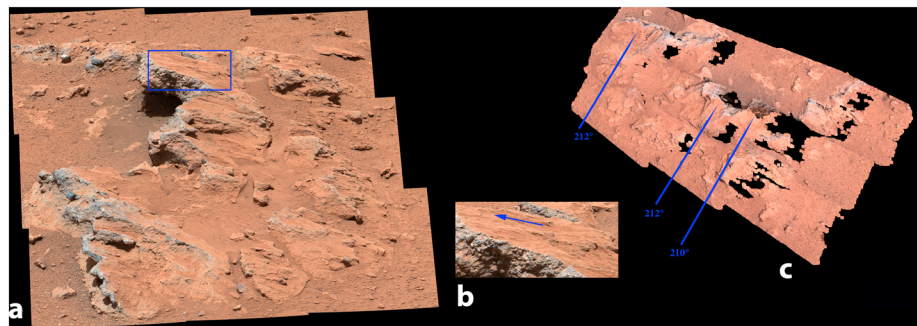

Figure 3. Hottah rock outcrop showing prominent faceting, grooves, and rock tails. (a) Mastcam right mosaic mcam00177, with the enlargement shown in Figure 3b outlined in blue. The arrows are directional trends closely matching those shown in Figure 3c. The viewing azimuth is 118°. (b) Enlarged portion of the blue box in Figure 3a. The arrow shows the trend of grooves on the rock facet and the inferred downwind direction. (c) Orthorectified overhead projection made by JPL's Operations Product Generation Subsystem group showing the inferred southwesterly upwind wind azimuth based on the orientation of the textural features and facets.
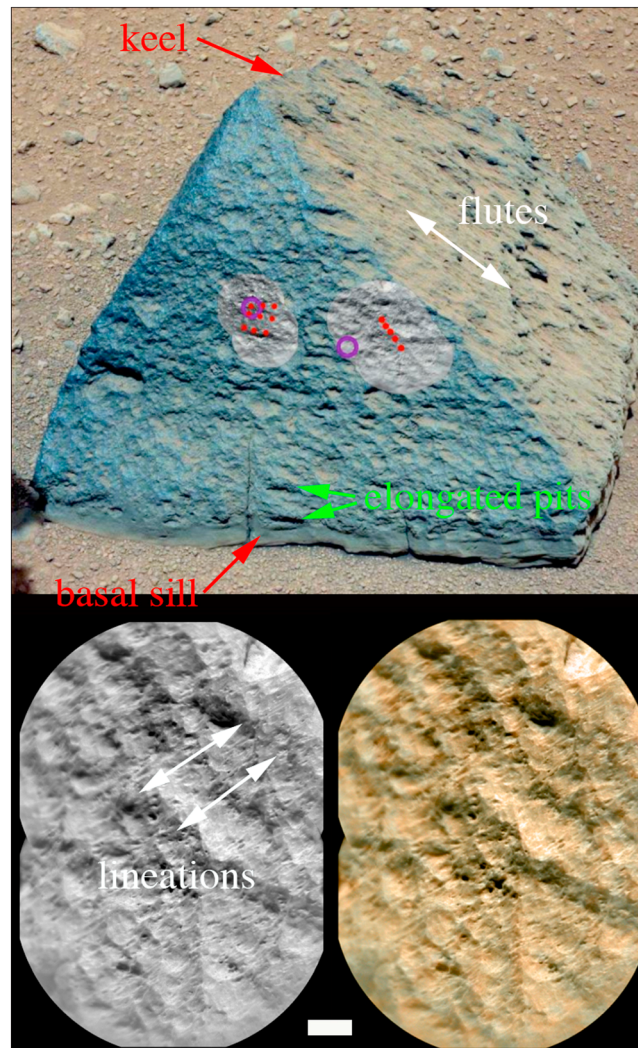
Figure 4. Jake rock. At left is a color Mastcam 34 image (ML_401573007EDR_S0042100AUT_04096M) with superposed RMI mosaics shown in grayscale and the location of LIBS spots as red dots (lithium peaks at 670.9 nm from the right-most raster are shown in Figure 12b). This view is along a pointing azimuth of ~116° (ESE), such that the right side facet is indicative of abrasion from southwesterly winds (Figures 1, 8, and 9). The rightmost RMI mosaic is enlarged at right. White scale bar equals 1 cm. Jake has the most prominent abrasion textures seen between Bradbury Landing and Rocknest, with a distinct keel at its crest, penetrating flutes, elongated pits, lineations, and a basal sill.

planetWRF model [*Richardson et al.*, 2007; *Toigo et al.*, 2012] that was developed from the National Center for Atmospheric Research's Earth-based Weather Research and Forecasting (WRF) model. MarsWRF solves the fully compressible Euler equations in flux form on an Arakawa C-grid with a terrain-following vertical coordinate. In these simulations the hydrostatic approximation was used and contains parameterizations of physical processes including radiative transfer through a dusty CO_2 atmosphere, exchange of heat and momentum between the atmosphere, surface and subsurface, the CO_2 condensation-sublimation cycle, and horizontal and vertical eddy mixing at scales smaller than the model's grid separation. A prescribed atmospheric dust distribution was used in MarsWRF that varies in space and time so as to mimic a year observed by the Mars Global Surveyor (MGS) Thermal Emission Spectrometer instrument with no major dust storms present (the "MGS scenario" described in *Richardson et al.* [2007]). MarsWRF also includes topography and surface roughness maps derived from the Mars Orbiter Laser Altimeter [*Smith et al.*, 2001] and surface thermal inertia and albedo maps from Mars Global Surveyor Thermal Emission Spectrometer data [*Christensen et al.*, 2001].

For this work, MarsWRF was run at a global resolution of 2° with three additional levels of "nesting" (i.e., smaller domains embedded inside each other with increased resolution from one to the next) over Gale
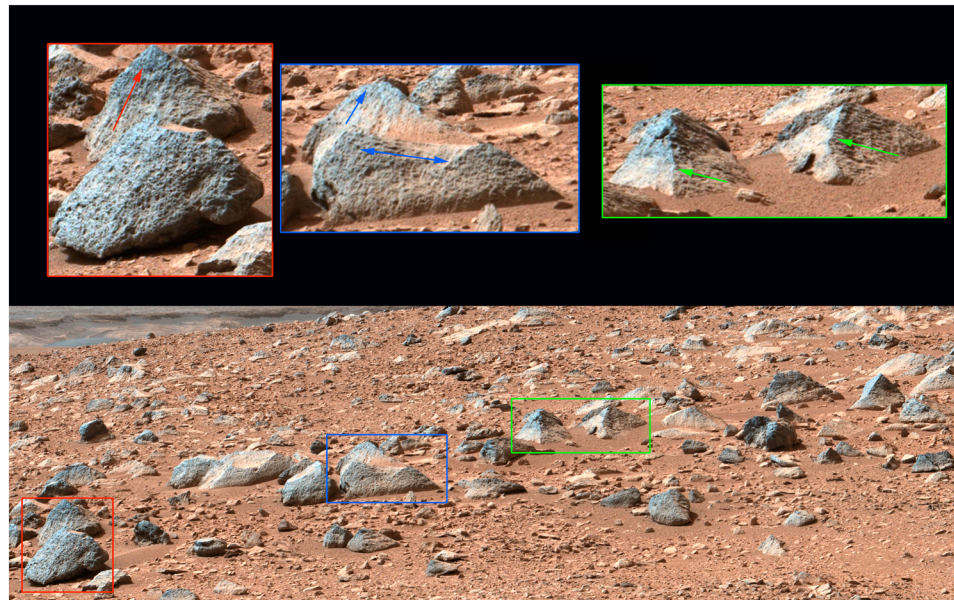
Figure 5. Portion of Mastcam right mosaic mcam00231 showing ventifacts in Cluster 2. The mosaic is pointed approximately at azimuth 140°. Here there is strong evidence for bidirectional flow, with ventifacts indicating winds coming from ~ NNE (~left-dipping facets and textures) and ~ SW (~right-dipping facets and textures; see lower right inset in Figure 1). Colored boxes are enlarged at the top, with arrows showing the downwind direction of inferred winds.

Crater. The innermost domain (domain 4) has a resolution of ~4 km, with 120 longitude and 120 latitude points, covering an area of nearly $9 \times 9°$ centered over the middle of Gale. To model the long-term wind regime at the MSL landing site, nested simulations were performed every 30° of L_s to capture the seasonal cycle, each lasting 13 Mars sols, though only the final 10 sols were used (to avoid spin-up effects). Near-surface wind vectors, air density, and friction speed (u^*) were output every minute. The resulting twelve 10 sol data sets were then weighted by the fraction of the year spent in each 30° L_s "season" and combined to provide a proxy for the annual wind field. In addition, by assuming that the input friction speed was that at threshold (u^*_t), the sand "drift potential," proportional to flux, was computed at each point as $u^{*2}(u^* - u^*_t)$ [*Fryberger and Dean*, 1979; *Tsoar*, 2001]. Finally, the net transport direction and the orientation that would be expected from any dunes predicted using the Gross Bedform-Normal Theory [*Rubin and Hunter*, 1987] was calculated and compared to the orientations of actual dunes to the southeast and the Rocknest sand shadow/drift.

Abrasion of possible surface alteration was assessed by plotting the intensity of the lithium peak from LIBS as a function of depth for the ventifact rock dubbed Jake Matijevic (hereafter referred to as "Jake"), one of the most distinctive ventifacts and an apparently unabraded portion of Bathurst Inlet. Only a few ventifacts were analyzed with LIBS between Bradbury Landing and Rocknest (A comprehensive assessment of coatings on rocks, irrespective of abrasion, can be found in *Ollila et al.* [2014].). It was therefore the intent of this analysis to compare two rocks that represent opposite ends of the spectrum of abrasion to see if any trends in chemical composition were apparent.

3. Results

3.1. Distribution

Ventifacts are found throughout the traverse from Bradbury Landing to Rocknest at the entrance to Yellowknife Bay (Sols 0–100) (Figure 1). As discussed below, it appears that about half the rocks studied are ventifacts. A total of 48 rocks had both ventifact characteristics and were close enough to the rover to get 3-D orientation data from stereo Navcam images (Table S1). Of these, 33 are float, 12 are probable outcrop, and 3 are definite outcrop. In addition, two rocks (Peacock Hills and Preble) were identified as ventifacts in RMI because of their microscale textures but were too small to measure feature orientations. The ventifacts are concentrated in three zones, centered on the landing point, a clump ~50 m WSW of Rocknest, and the
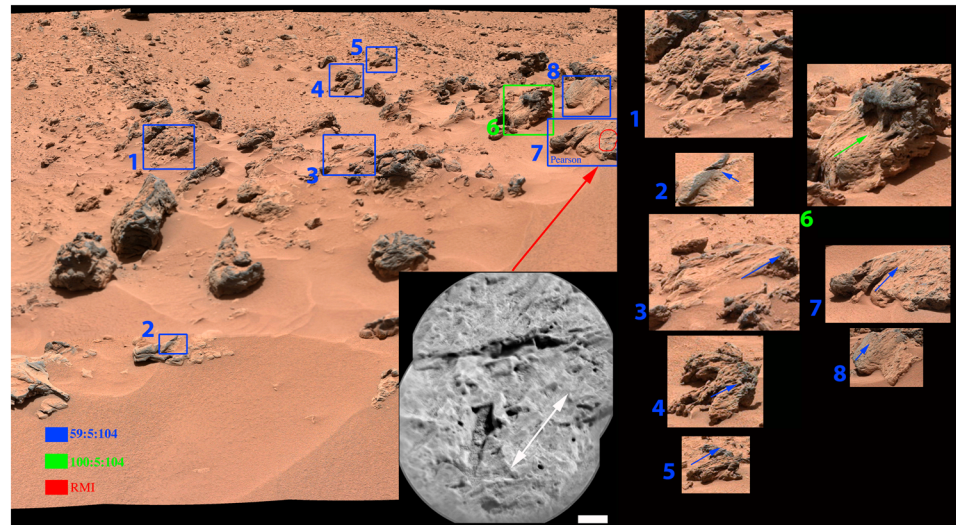
Figure 6. Portion of Mastcam left mosaic mcam00296 showing ventifacts in the Rocknest region that encompass ventifact Cluster 3. Blue and green boxes reference the Navcam mosaic used to derive inferred wind orientations. These are enlarged at right, with the arrows pointing in the inferred downwind direction. The Mastcam mosaic is pointed approximately due north (azimuth = 0°). Note that except for the fluting on the small rock at lower left, the orientations are from lower left to upper right, indicating winds from the southwest. The red outline shows the location of the RMI mosaic of Pearson, at the lower right. Scale bar is 1 cm. Note the submillimeter lineations in the RMI image and their alignment (indicated by double-sided white arrow) with the coarser flutes seen in Mastcam data.

Rocknest region itself at the margin of Yellowknife Bay (hereafter referred to as C(cluster)1, C2, and C3, respectively). Ventifact distribution is sparse between Bradbury Landing and the other zones, limited to the Hottah outcrop, the rock Jake, and rocks seen on Sol 49. The mapped ventifact distribution is dictated not only by the location of rocks, in general, but also by nongeological factors such as the location of the rover
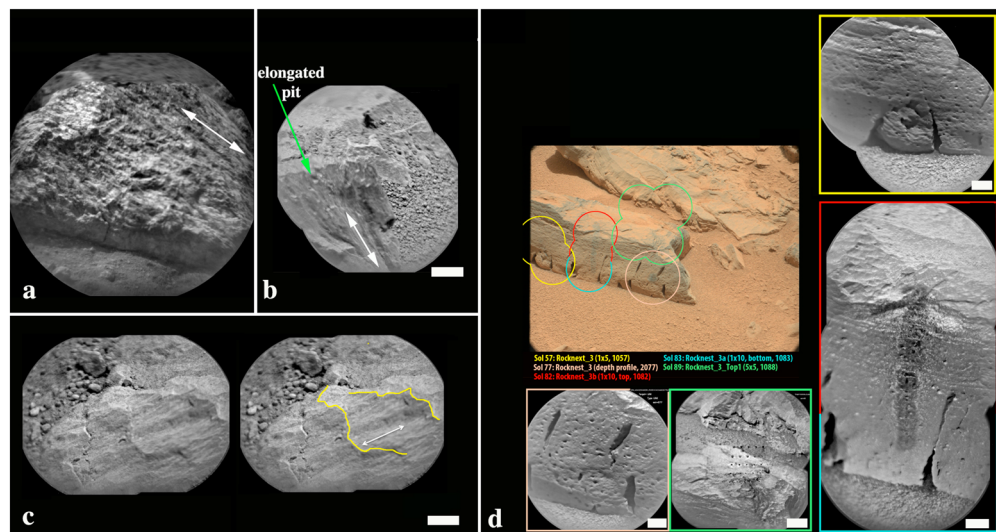

Figure 7. Rock RMI images showing small-scale ventifact textures. White scale bar is 1 cm. (a) Peacock Hills rock. Fluted texture is oriented from upper left to lower right (indicated by bidirectional arrow). (b) RMI image of Rocknest 6 rock (foreground). Elongated pits with major axis pointed to "11 o'clock" are aligned with the lineations, indicating a common direction of sand-laden winds. (c) RMI image mosaic of Preble rock. Here the high resolution reveals both scallops and abrasion lineations within the flutes. Interpretive outlines of a scallop edge are shown in yellow at the right, with the double-sided arrow indicating lineation trends. (d) Mastcam context right image (0086MR0375000000E1; azimuth ~266°) and RMI images and mosaics of Rocknest 3. Outline color of RMI images correlates to the location in the Mastcam image. The dark band in the RMI image at the right is the result of LIBS ablation of dust off the rock.
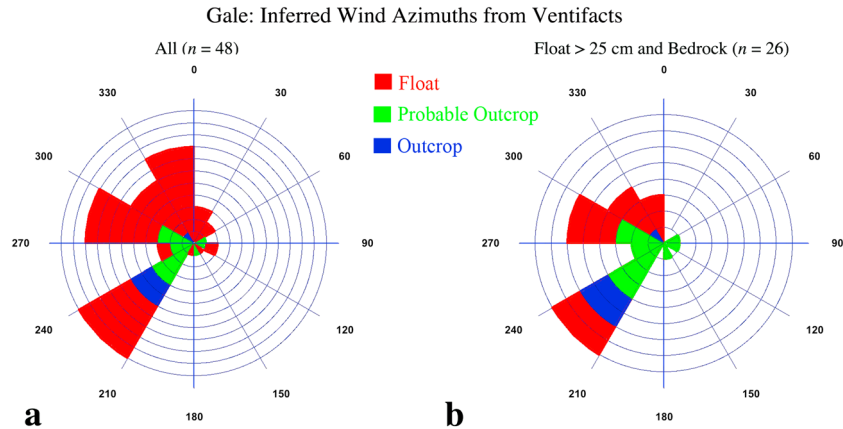
Gale: Inferred Wind Azimuths from Ventifacts

Figure 8. Upwind directions inferred from the orientation of ventifact facet dip slopes and texture orientations. Float rocks, probable outcrop, and definite outcrop are color coded. (a) All rocks. (b) Restriction to float > 25 cm and bedrock. These are more reliable indicators of formative winds, as small rocks can be moved over time (see Figure 9).

traverse path and image coverage. In many cases, rocks that looked like ventifacts were seen in the images, but definitive identification and derivation of orientation was not possible because they were too small or far away. Were RMI or MAHLI coverage more extensive, then a greater number of ventifacts might be found. All the ventifacts from Sols 0–100 are within the "smooth hummocky" geomorphic unit mapped using HiRISE images [*Calef et al.*, 2013]. In a general clast survey from Bradbury to Rocknest using Mastcam, all the ventifacts were classified as "Type 1" clasts that are defined as gray, with or without a tan patina or coating, and comprising 60–80% of pebble to cobble sizes rocks along the traverse [*Yingst et al.*, 2013].

The areas near ventifacts in C1 and through the Sol 49 point in the traverse lack prominent sand deposits, whereas those in C2 and in particular C3 are located near or within drifts. C3 is adjacent to the Rocknest "sand shadow" that was investigated in situ by the arm-mounted instrument suite then scooped, with samples analyzed by the Chemistry and Mineralogy and Sample Analysis at Mars instruments [*Blake et al.*, 2013]. MAHLI, Mastcam, and RMI images of the sand shadow surface and trenched section show a top surface armored with a crust of ~ 1 mm coarse sand grains overlying a core of ~ <200 μm sand, evidence for an inactive aeolian surface [*Goetz et al.*, 2013; *Kocurek et al.*, 2013]. In summary, there is no evidence for active aeolian bedforms where the ventifacts are found.
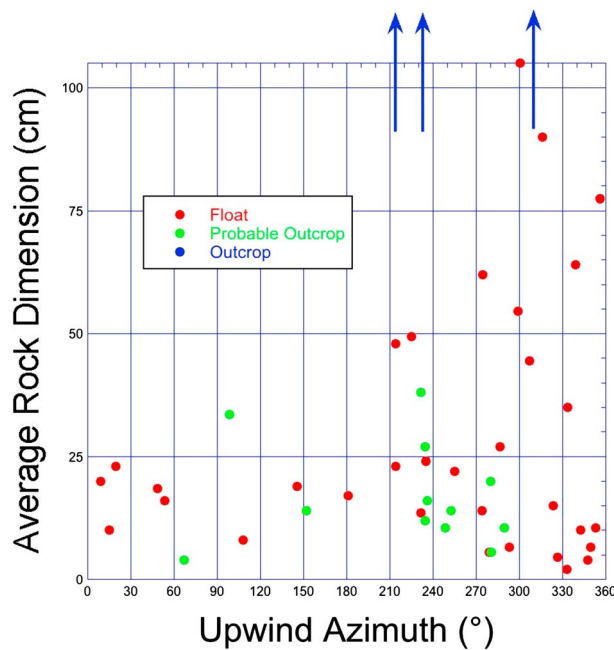

Figure 9. Average rock dimension (mean of height and width) versus upwind azimuth of ventifacts. Bedrock, which does not have a diagnostic scale, is indicated by the blue arrows. The plot indicates that the largest rocks and bedrock show upwind azimuths from the southwest (see Figure 8).

3.2. Ventifact Characteristics

The 50 ventifacts contain one or more diagnostic features and textures: facets (39 rocks, 78% of sample), keels (12, 24%), basal sills (3, 6%), elongated pits (9, 18%), scallops/flutes (36, 72%; because of their transitional nature, they are grouped as one category), grooves (13, 26%), rock tails (3, 6%), and lineations (5, 10%). (Figures 2–7 and Table S1). These statistics are selectively
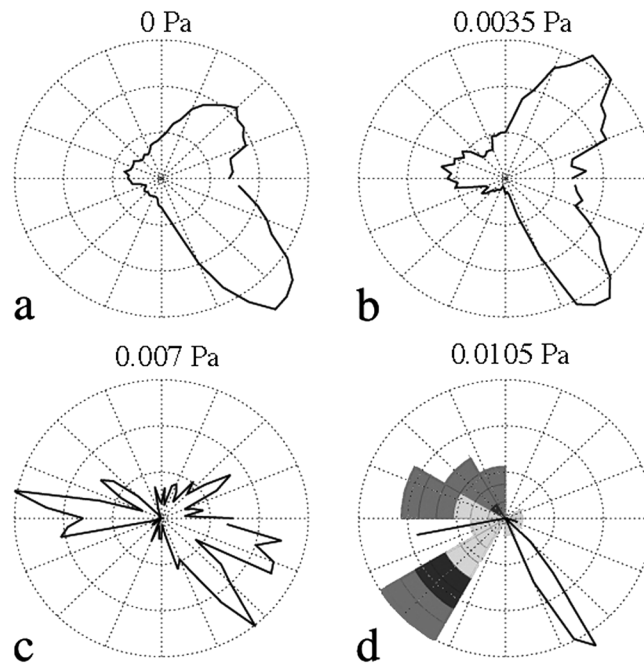
Figure 10. (a–d) Relative fractions of predicted wind shear stresses above the given shear stress over a Mars year shown as upwind azimuth. The location is centered on the MSL landing site (137.444°E, 4.55°S), with a resolution of ~4 km. The plots are normalized to themselves but not to the other plots. The predicted fluid threshold for fine sand on Mars of ~0.045 Pa is never reached, although the impact threshold of 4.5×10^{-4} Pa is commonly exceeded (i.e., between Figures 10a and 10b). The upwind directions indicated by large float and bedrock ventifacts as displayed in Figure 8b is overlaid on Figure 10d in order to compare the rock record with the wind predictions. See Figure S1 for grid points northwest and southwest of MSL.

biased by imaging opportunities and resolution. For example, lineations are only identified in RMI and MAHLI images because of the high resolution of these cameras. However, they demonstrate that the full suite of characteristics found on terrestrial ventifacts is also seen in Gale Crater. In addition, although keels were identified, the mapping of multiple facet directions was commonly limited by simple image geometry. For the data in this study, the rover was driving predominantly on a west to east path, biasing imaging to west facing portions of rocks, and thereby the identification of ventifact features formed from westerly winds. The average size (mean of width and height measured in MSLICE) of ventifact float rocks ranges from 2 to 105 cm, whereas the surface exposures of probable outcrops ranges from 4 to 38 cm. Abraded portions of definite outcrops have no characteristic size because they are part of a larger rock expanse.

Wherever a range of imaging scales is available for the ventifacts, the highest-resolution data, generally from RMI and MAHLI, consistently show evidence for abrasion in the form of microscale lineations. For example, Jake shows centimeter-scale flutes in Mastcam images and submillimeter-scale lineations in RMI and MAHLI images (Figure 4). Similarly, RMI images show lineations aligned within coarser scallops and flutes on Preble, Rocknest 6, Pearson, and Rocknest 3 (Figures 6 and 7).

3.3. Ventifact Orientations

The rose diagram of ventifact-derived wind azimuths shows inferred winds from all 30° bins but with a strong bias to westerly flow (38 measurements or 79% percent of sample), with the strongest trend in the 210–240° bin (11 measurements; 23% of sample, 29% of westerly sample) (Figure 8a). There is an apparent separation between northwesterly (270–360°) and southwesterly (210–240°) statistics, with only three rocks in the 240–270° bin. In comparing the average rock dimension versus azimuth, it is seen that the greatest spread in azimuths is found for rocks less than 25 cm in average dimension (Figure 9). Of these, 22 are float rocks, and it is possible that because of their small size, they could have (1) shifted during or following the period over which their abrasion textures formed, thereby giving erroneous data on wind direction or (2) been abraded by winds more affected by microtopography than larger rocks. Removing these from the statistics leaves only three rocks with easterly (0–180°) azimuths, such that 88% (23/26) indicate abrasion from westerly flow (Figure 8b).

3.4. Wind Models

Plotting predicted winds at the grid point closest to the MSL landing site (137.444°E, 4.55°S) for shear stresses greater than 0 Pa (all winds) shows directions predominantly from the northeast and southeast (Figure 10a), a trend approximately reproduced for stresses of > 0.0035 Pa (friction speed [$u*$] of 0.42 m s^{-1} for an atmospheric density of 0.02 kg m^{-3}; Figure 10b). At stresses above 0.007 Pa (0.59 m s^{-1}), winds are
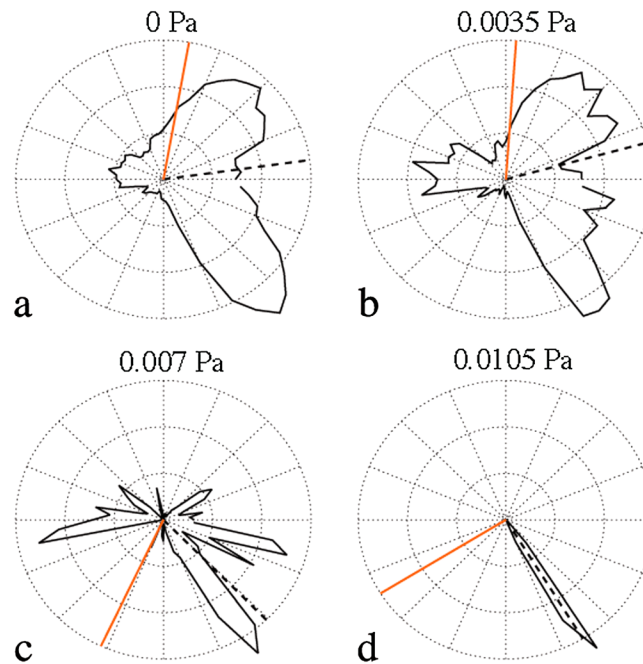
Figure 11. (a–d) Wind roses converted to sand drift potential by assuming the given shear stress is equivalent to that for saltation threshold (shown as solid black outlines). The net upwind transport direction and the orientation that would be expected from any dunes predicted using the Gross Bedform-Normal Theory [*Rubin and Hunter*, 1987] are shown as the dotted black and solid orange line, respectively. The predicted fluid threshold for fine sand on Mars of ~0.045 Pa is never reached, although the impact threshold of 4.5×10^{-4} Pa is commonly exceeded (i.e., between Figures 11a and 11b). As such, these plots should serve as illustrations for potential sand movement only. See Figure S2 for grid points northwest and southwest of MSL.

bidirectional, westerly and easterly (Figure 10c), and above 0.0105 Pa (0.72 m s^{-1}) they are predominantly southeasterly (Figure 10d). The highest stress reached is 0.0165 Pa. These stresses compare to estimates of impact threshold (the stress at which the movement of particles ejected by impact splash can be sustained by the flow) and fluid threshold (at which the wind initiates particle motion) stresses for 150–250 μm basaltic sand on Mars of 4.5×10^{-4} Pa (u* = 0.15 m s^{-1}) and 0.045 Pa (u* = 1.5 m s^{-1}), respectively [*Iversen and White*, 1982; *Kok et al.*, 2012]. Therefore, winds at the fluid threshold needed to initiate sand motion are not predicted, although the impact threshold is met. Grid points northwest of MSL show similar behavior, whereas those to the southwest lack prominent easterly and westerly flow, being dominated by southeasterly winds (Figure S1). The sand drift potential shows trends like that of the predicted winds shown in Figure 10 but with a greater sensitivity to

high shear stresses because it is proportional to flux that is parameterized as $u*^2(u* - u*_t)$ (Figure 11). The net upwind transport direction is easterly for threshold stresses less than 0.0035 Pa and southeasterly for 0.007 and 0.0105 Pa. Dune orientations predicted from the Gross Bedform-Normal Theory [*Rubin and Hunter*, 1987] at the highest shear stress of 0.0105 Pa (closest, but not at fluid threshold) predict dune crest lines oriented SW-NE from a southeasterly wind (Figure 11d). In contrast, the Rocknest sand shadow/drift, near cluster C3, is oriented ~ N-S and thought to have formed by northerly winds [*Kocurek et al.*, 2013]. As is the case at the MSL grid point, the sand drift potentials for areas NW and SW of MSL (Figure S2) mirror the predicted winds but with a greater sensitivity to high wind speeds because of the flux equation. Predicted dune orientations show a range of azimuths, depending on the grid point (Note, however, that these are predictions of where dunes should be present if they exist; in this region of Gale Crater, although ripples and drifts are found, there are no dunes.). At face value, these models predict that winds should never entrain sand into saltation (the fluid threshold), although it could be sustained in motion once moving (the impact threshold). Studies of dune and ripple orientations and displacement in the barchans field southwest of the MSL landing site indicate strong bidirectional winds from the NW and ENE, with mesoscale modeling indicating a dominance of ENE winds in the dune field [*Silvestro et al.*, 2012]. Similarly, the direction of scarp retreat and rock tails in Yellowknife Bay to the northeast of Rocknest is consistent with northeasterly winds that, based on cosmic ray exposure ages, occurred 78 ± 30 Ma [*Farley et al.*, 2014]. The ventifact trends that require a predominance of northwesterly-southwesterly flow are not predicted by the wind models, ENE bed form orientations, and Yellowknife results, but are consistent with the NW bedform orientations.

3.5. Lithium Versus Depth From LIBS

Aeolian abrasion could erase vestiges of rock chemical weathering rinds or coatings if the rate of removal exceeds that of surface alteration development or postdates rind/coating development. Lithium, a highly
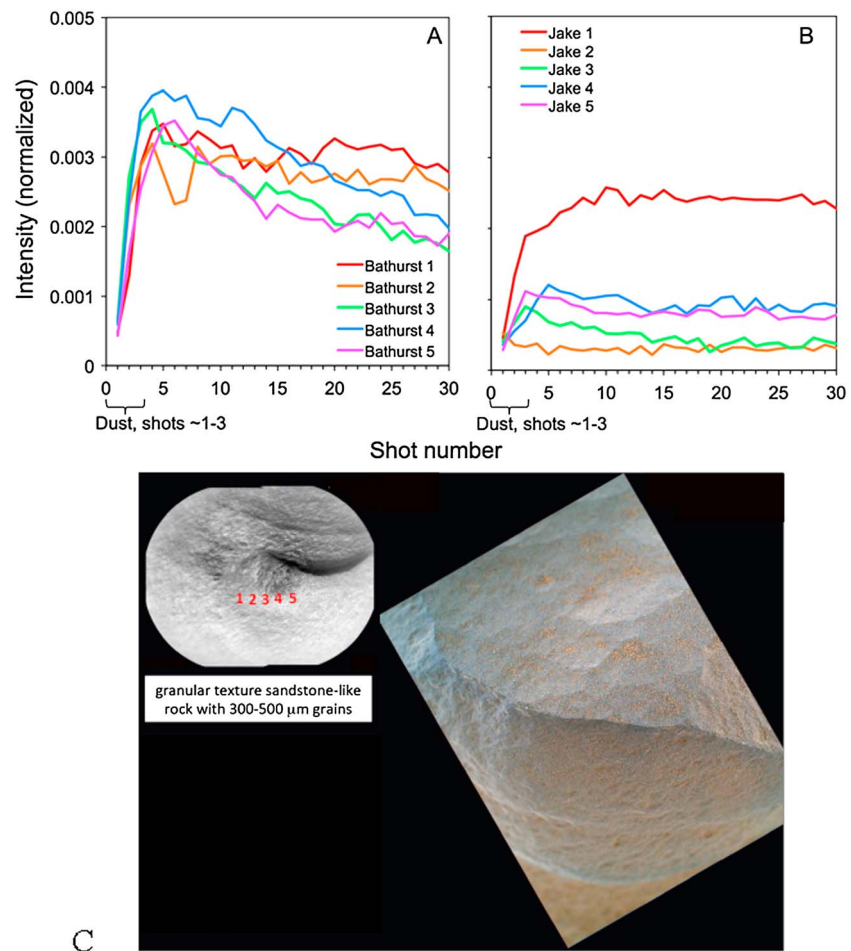
Figure 12. Trends in lithium abundance with depth for the relatively unabraded rock Bathurst Inlet and the ventifact Jake. (a) Intensity of the Li peak at 670.9 nm as a function of shot for the five rastered points of Bathurst Inlet (Sol 55). After surface dust has been cleared in the first approximately three shots, a distinctly decreasing trend with depth in each sampling location is seen (particularly points 3–5), suggesting the presence of surface alteration in a Li-rich rind. This target has the highest concentrations of Li observed in the first 360 sols of the mission [*Ollila et al.*, 2014]. (b) Intensity of the Li peak at 670.9 nm as a function of shot for the five rastered points of Jake (Sol 55). Once the surface dust is removed in the first approximately three shots, the Li peak remains constant with depth, suggesting a lack of surface alteration, with the possibility that the rate of abrasion exceeds that of rind development. Point 1 has higher Li than the others, with a modeled abundance of ~45 ppm [*Ollila et al.*, 2014]. The location of the LIBS measurements for this analysis is the rightmost raster seen in Figure 4 (top). (c) RMI data (left) with the location of LIBS points and MAHLI view (right) of Bathurst Inlet. Note the less developed abrasion textures compared to Jake (only subtle etched layers and fluting) (Figure 4).

fluid mobile element that is commonly enriched within clays [*Starkey*, 1982], is also found in the clay component of rock varnishes, suggesting that it can be concentrated on rock surfaces through alteration of airfall dust from atmospheric moisture [*Thiagarajan and Lee*, 2004]. As such, Li can be an important tracer for the action of frost or water films. Easily detected by ChemCam, it has been found enriched on rock surfaces during the first part of the Curiosity traverse, suggesting aqueous alteration on Mars [*Ollila et al.*, 2014]. Intensity at the 670.9 nm lithium line for 5 LIBS observation points each on Bathurst Inlet, and Jake show clear differences as a function of depth for shots 4–30, beneath the dust cover (Figure 12). Whereas line intensity in Bathurst, particularly raster points 3–5, decreases with depth, all five of the Jake points remain more or less constant, even point 1 that exhibits higher overall Li. The LIBS points on Jake are located on a rough surface with elongated pits that are characterized by abrasion subparallel to the surface (Figure 4). The LIBS points on Bathurst Inlet are on a smooth surface that qualitatively appears less abraded (Figure 12c).

4. Discussion

The findings that provide greatest insight on the geologic history of the MSL landing region are the following: (1) Evidence of abrasion is found at a range of scales; (2) Some rocks lack evidence for abrasion; (3) Ventifacts are distributed throughout the traverse, which includes regions with indurated (inactive) sand bedforms and shadows and areas lacking any sand deposits where deflation may have occurred; and (4) The ventifacts were formed by predominantly westerly winds, perhaps divided into two main components, in contrast to wind model predictions and, for the SW component, regional dune orientations. We address each of these points in turn, compare them to other Martian landing sites, and then integrate these results into a model for wind processes over time in the Bradbury-Rocknest region, with implications for Mars overall.

In all cases, rocks identified as ventifacts in Mastcam/Navcam also show textures at finer scales in RMI and MAHLI images. Therefore, the fraction of ventifacts along the Sol 0–100 traverse can be roughly gauged by considering targets for which both high-resolution RMI and coarser-scale Mastcam and Navcam images are available. Through Sol 100, RMI imaged 32 rocks or rock-soil mixtures, of which nine have distinctive ventifact attributes that are used in the data for this paper (the rocks Coronation, Mara, Peacock Hills, Thor Lake, Preble, Jake, Rocknest 6, Pearson, and Rocknest 3), 12 have textures that could be from wind abrasion or have other origins, and the remaining 11 are inconsistent with ventifacts. This suggests that ventifacts can be identified based on the presence of fine-scale textures such as lineations and small scallops and flutes, in which case the RMI data indicate that about half of the rocks along the traverse have been abraded (i.e., nine definite ventifacts and 21 definite plus possible candidates out of 32 RMI rock images indicates ~1/3 to 2/3 of rocks are ventifacts). This is qualitatively consistent with rocks seen in Mastcam images, although a detailed statistical study has not been done.

The colocation of apparently unabraded rocks with ventifacts could be caused by abrasion shielding and enhancement. For example, field relationships on Earth can be complex, with upwind rocks, commonly with associated sand ramps, causing saltating grains to bounce to high elevations, effectively shielding low-lying rocks from particle collisions and causing greater abrasion higher up [*Laity and Bridges*, 2009]. Another cause could be spatial and temporal variability in burial and exhumation. Regional-scale results from mapping of Gale strata and geomorphic relationships indicate infill followed by exhumation [*Malin and Edgett*, 2000], a process that may have included the plains surrounding the present-day central mound (Mount Sharp/Aeolus Mons). If the Bradbury-Rocknest area was covered and then exhumed, many or all rocks would have been shielded from abrasion for some amount of time. It is also possible that hardness differences among rocks could affect abrasion susceptibility. Finally, some rocks may have been transported to the site, most likely as impact ejecta, after major abrasion ceased. All of these mechanisms could lead to the coexistence of abraded and apparently unabraded rocks in the same area.

Ventifacts are distributed throughout the traverse, which includes those near the indurated (inactive) coarse grain-coated Rocknest sand shadow (Figure 6) [*Kocurek et al.*, 2013; *Goetz et al.*, 2013] and areas lacking any sand deposits. Some rocks, such as Jake, a large (~half a meter) rock seen in the middle of the traverse in a sand-free area, have basal sills indicative of soil deflation (Figure 4). This indicates that fine, loose particles have been removed from this region, leaving behind remnant rocks and indurated bedforms. Evidence for deflation is consistent with the burial and exhumation hypothesis.

HiRISE images do not show any dark sand dunes in this area, in contrast to the large dune field ~2.6 km to the south that shows evidence for current migration by winds from the NW and ENE [*Silvestro et al.*, 2012]. Because significant rock abrasion requires the presence of saltating sand [*Laity and Bridges*, 2009], these observations suggest that ventifact formation occurred during periods in the past when sand was more plentiful locally. One possibility is that sand migration pathways have varied over time and once passed through the Bradbury-Rocknest region. Alternatively, a fresh supply of sand could have been delivered by the Peace Vallis alluvial fan whose margin is near this area [*Palucis et al.*, 2013]. This supply-limited sand source would abrade rocks before subsequently becoming depleted or indurated.

The rose diagrams (Figure 8) suggest two predominant wind regimes: one from the northwest and the other from the southwest. The former is consistent with one of the two modern bidirectional wind components (the other being from the ENE) identified as formative to the dark dune field to the south [*Silvestro et al.*, 2012]. This could indicate that the NW trend is long lived and the SW one older. However, in looking at the detailed spread in derived azimuths (Figure 9), the lack of trends in the rose's 240–270° range may simply be a

sampling artifact. Therefore, the most conservative interpretation is that there is a predominant westerly component. Determining whether two components exist requires a greater sampling size. This will be possible in future studies of ventifacts along the traverse from Rocknest toward Mount Sharp.

The ventifact-derived westerly wind vectors and their disagreement with model predictions, some barchans orientations, and results reported for Yellowknife Bay [*Farley et al.*, 2014] for easterly high-speed winds can be explained in several ways. It may very well be that ventifacts from easterly winds exist along the traverse but that the predominant eastward rover path (so viewing mostly west facing rock faces) biases the statistics. In this case, the problem is not so much the difference between the ventifact and model results but rather how to explain the westerly flow that is not predicted by the models. Appealing to differences in past wind directions is challenged by research showing that obliquity changes have minimal effect on wind patterns [*Fenton and Richardson*, 2001], such that the eastward flow occurring today likely existed in the past.

More likely, the models fail to show extremely rare events in which the majority of saltation and sand transport takes place, regardless of time period. Indeed, the models do not predict any winds above the fluid threshold value of ~0.045 Pa. Ventifacts on Earth align with only the highest-speed winds [*Bridges et al.*, 2004], but threshold is reached much more commonly on Earth than on Mars [*Kok et al.*, 2012]. Abrasion is increasingly more effective the greater the wind speed above threshold, as the energy imparted by impacting particles varies in proportion to the square of the velocity. It may therefore be that typical winds in this region do little work on rock surfaces, with significant abrasion instead confined to infrequent yet powerful events that occasionally occur from the west. Any such rare winds would be particularly effective under past obliquity conditions. Although not changing directions significantly, variations in precession and eccentricity in the modern epoch can change the magnitude of near-surface winds [*Haberle et al.*, 2003], with higher obliquities potentially releasing CO_2 trapped in the southern cap and regolith, increasing atmospheric pressure up to 10–15 mbar compared to the present ~6 mbar [*Kieffer and Zent*, 1992; *Philipps et al.*, 2011]. Such an increase would lower threshold friction speeds by 30–60% (as friction speed is proportional to the square root of pressure). Therefore, it may be that the rates of sand abrasion, along with wind deflation [*Armstrong and Leovy*, 2005], are cyclical and peak in higher obliquity periods.

Arguing against this hypothesis is the apparent absence of a lithium-rich alteration LIBS signature on Jake that is found on a relatively unabraded portion of Bathurst Inlet, suggesting that that the rate of abrasion exceeds that of surface alteration or that the processes occurred at different time. However, given that the rate of chemical alteration is poorly constrained, the unknown original Li abundances of these rocks, and the preliminary nature of these comparisons, it is difficult to make firm conclusions until more statistics are compiled, which should be possible further along Curiosity's traverse.

Some insight into the relative merits of these ideas can be gleaned from consideration of ventifacts at the other three rover sites. Similar to the results here, the orientation of the Pathfinder ventifacts and locally eroded crater rims are inconsistent with current wind predictions and bedform orientations, and it was proposed that they were formed by paleowinds shortly after Ares Valles debouched fresh sand in the region [*Bridges et al.*, 1999; *Greeley et al.*, 2000]. Ventifacts along Spirit's traverse from the landing point on the floor of Gusev Crater up through the Columbia Hills are consistent with current wind patterns [*Greeley et al.*, 2008], but within the Columbia Hills themselves are judged as largely reflective of winds funneled through topography, principally the troughs of major ripple sets [*Thomson et al.*, 2008]. Rock tails within the soft sulfate-rich sandstones of Meridiani Planum viewed by Opportunity have trends consistent with current and fossil ripples and a wind streak [*Sullivan et al.*, 2005]. In summary, the wind trends indicated by ventifacts can be interpreted in several ways depending on the results and local geology.

As of this writing, Curiosity has not yet reached Mount Sharp, and data past Sol 100 have not been thoroughly studied for evidence of wind abrasion. Future results will provide additional information on the questions raised here, principally the extent, timing, and wind directions associated with major abrasion in Gale Crater. For example, within Yellowknife Bay [*Farley et al.*, 2014] and farther along the traverse, many outcrops are clastic sedimentary rocks such as sandstones and mudstones that are likely lower in abrasion resistance compared to basaltic lithologies and therefore more sensitive to shorter timescales and lower energy saltation. As Curiosity gets close to and then passes through the Gale dune field, ventifacts will likely be reflective of recent or current sand migration, and mixtures of fossil and active ventifacts may be found at the periphery of the modern sand transport corridor. Major effects on wind flow from the topography of

Mount Sharp will likely form complex patterns in areas that sand has passed through. In any case, the results so far, from just the beginning of Curiosity's mission, point to rock abrasion being a major geomorphic agent in Gale Crater.

References

Aghevli, A., et al. (2006), Planning application for three Mars missions with Ensemble, 5th International Workshop on Planning and Scheduling for Space.

Anderson, R. B., and J. F. Bell (2010), Geologic mapping and characterization of Gale Crater and implications for its potential as a Mars Science Laboratory landing site, *Mars*, *5*, 76–128.

Anderson, R. S. (1986), Erosion profiles due to particles entrained by wind: Application of an eolian sediment-transport model, *Geol. Soc. Am. Bull.*, *97*, 1270–1278.

Armstrong, J. C., and C. B. Leovy (2005), Long term wind erosion on Mars, *Icarus*, *176*, 57–74.

Bishop, D. G., and D. C. Mildenhall (1994), The geological setting of ventifacts and wind-sculpted rocks at Mason Bay, Stewart Island, and their implications for late Quaternary paleoclimates, *N. Z. J. Geol. Geophys.*, *37*, 169–180.

Blackwelder, E. (1929), Sandblast action in relation to the glaciers of the Sierra Nevada, *J. Geol.*, *37*, 256–260.

Blake, D. F., et al. (2013), Curiosity at Gale Crater, Mars: Characterization and analysis of the Rocknest sand shadow, *Science*, *341*, 1,239,505, doi:10.1126/science.1239505.

Breed, C. S., J. F. McCauley, and M. I. Whitney (1989), Wind erosion forms, in *Arid Zone Geomorphology*, edited by D. S. G. Thomas, pp. 284–307, Belhaven Press, London.

Bridges, N. T., and J. E. Laity (2013), Fundamentals of aeolian sediment transport: Aeolian abrasion, in *Treatise on Geomorphology*, Aeolian Geomorphology, vol. 11, edited by J. Shroder et al., pp. 134–148, Academic Press, San Diego, Calif.

Bridges, N. T., R. Greeley, A. F. C. Haldemann, K. E. Herkenhoff, M. Kraft, T. J. Parker, and A. W. Ward (1999), Ventifacts at the Pathfinder landing site, *J. Geophys. Res.*, *104*, 8595–8615, doi:10.1029/98JE02550.

Bridges, N. T., J. E. Laity, R. Greeley, J. Phoreman, and E. E. Eddlemon (2004), Mechanisms of rock abrasion and ventifact formation from laboratory and field analog studies with applications to Mars, *Planet. Space Sci.*, *52*, 199–213.

Bridges, N. T., et al. (2012a), Planet-wide sand motion on Mars, *Geology*, *40*, 31–34.

Bridges, N. T., F. Ayoub, J.-P. Avouac, S. Leprince, A. Lucas, and S. Mattson (2012b), Earth-like sand fluxes on Mars, *Nature*, *485*, 339–342.

Calef, F. J., et al. (2013), Geologic mapping of the Mars Science Laboratory landing ellipse, *Lunar Planet. Sci.*, *XLIV*, 2511.

Chojnacki, M., D. M. Burr, J. E. Moersch, and T. J. Michaels (2011), Orbital observations of contemporary dune activity in Endeavour Crater, Meridiani Planum, Mars, *J. Geophys. Res.*, *116*, E00F19, doi:10.1029/2010JE003675.

Christensen, P. R., et al. (2001), Mars Global Surveyor Thermal Emission Spectrometer experiment: Investigation description and surface science results, *J. Geophys. Res.*, *106*, 23,823–23,871, doi:10.1029/2000JE001370.

Crockett, T., K. Shams, and J. R. Morris (2011), Telerobotics as programming, IEEE IEEECA paper#1489.

Dorn, R. I. (1998), *Rock Coatings*, 429 pp., Elsevier, Amsterdam.

Edgett, K. S., et al. (2009), The Mars Science Laboratory (MSL) Mars Hand Lens Imager (MAHLI) flight instrument, *Lunar Planet. Sci.*, *XL*, 1197.

Farley, K. A., et al. (2014), In situ radiometric and exposure age dating of the Martian surface, *Science*, *343*, 1,247,166.

Farr, T., and J. B. Adams (1984), Rock coatings in Hawaii, *Geol. Soc. Am. Bull.*, *95*, 1077–1083.

Fenton, L. K., and M. I. Richardson (2001), Martian surface winds: Insensitivity to orbital changes and implications for aeolian processes, *J. Geophys. Res.*, *106*, 32,885–32,902, doi:10.1029/2000JE001407.

Fryberger, S. G., and G. Dean (1979), Dune forms and wind regime, in *A Study of Global Sand Seas*, USGS Prof. Paper 1052, edited by E. D. McKee, pp. 137–170, U.S. Government Printing Office, Washington, D. C.

Goetz, W., et al. (2013), Morphological and chemical characteristics of sediment in the Rocknest eolian sand shadow, Gale Crater, Mars, *Lunar Planet. Sci.*, *XLIV*, 1222.

Gomez-Elvira, J., et al. (2011), Rover environmental monitoring stations for MSL mission, 4th International Workshop on the Mars atmosphere: Modeling and observations.

Greeley, R., M. D. Kraft, R. O. Kuzmin, and N. T. Bridges (2000), Mars Pathfinder landing site: Evidence for a change in wind regime from lander and orbiter data, *J. Geophys. Res.*, *105*, 1829–1840, doi:10.1029/1999JE001072.

Greeley, R., et al. (2006), Gusev crater: Wind related features and processes observed by the Mars Exploration Rover Spirit, *J. Geophys. Res.*, *111*, E02S09, doi:10.1029/2005JE002491.

Greeley, R., et al. (2008), Columbia Hills, Mars: Aeolian features seen from the ground and orbit, *J. Geophys. Res.*, *113*, E06S06, doi:10.1029/2007JE002971.

Haberle, R. M., J. R. Murphy, and J. Schaeffer (2003), Orbital change experiments with a Mars general circulation model, *Icarus*, *161*, 66–89.

Hansen, C. J., et al. (2012), Seasonal erosion and restoration of Mars' northern polar dunes, *Science*, *331*, 575–578.

Hoare, P. G., C. R. Stevenson, and S. P. Godby (2002), Sand sheets and ventifacts: The legacy of aeolian action in west Norfolk, UK, *Proc. Geol. Assoc.*, *113*, 301–317.

Iversen, J. D., and B. R. White (1982), Saltation threshold on Earth, Mars, and Venus, *Sedimentology*, *29*, 111–119.

Kieffer, H. H., and A. P. Zent (1992), Quasi-periodic climate change on Mars, in *Mars*, edited by H. H. Kieffer et al., pp. 1180–1218, Univ. of Arizona Press, Tucson.

Kite, E. S., K. W. Lewis, M. P. Lamb, C. E. Newman, and M. I. Richardson (2013), Growth and form of the mound in Gale Crater, Mars: Slope wind enhanced erosion and transport, *Geology*, *41*, 543–546.

Knight, J. (2008), The environmental significance of ventifacts: A critical review, *Earth Sci. Rev.*, *86*, 89–105.

Kocurek, G., N. Bridges, K. S. Edgett, W. Goetz, K. W. Lewis, M. B. Madsen, D. M. Rubin, R. J. Sullivan, and the MSL Science Team (2013), Rocknest sand shadow at the Curiosity field site: Morphology, origin, and stabilization, *Lunar Planet. Sci.*, *XLIV*, 1375.

Kok, J. F., E. J. R. Parteli, T. I. Michaels, and D. Bou Karam (2012), The physics of wind-blown sand and dust, *Rep. Prog. Phys.*, *75*, 106,901.

Kraft, M. D., and R. Greeley (2000), Rock coatings and aeolian abrasion on Mars: Application to the Pathfinder landing site, *J. Geophys. Res.*, *105*, 15,107–15,116, doi:10.1029/1999JE001229.

Laity, J. E. (1987), Topographic effects on ventifact development, Mojave Desert, California, *Phys. Geogr.*, *8*, 113–132.

Laity, J. E. (1994), Landforms of aeolian erosion, in *Geomorphology of Desert Environments*, edited by A. D. Abrahams and A. J. Parsons, pp. 506–535, Chapman and Hall, London.

Laity, J. E. (2009), Landforms, landscapes, and processes of aeolian erosion, in *Geomorphology of Desert Environments*, 2nd ed., edited by A. J. Parsons and A. D. Abrahams, pp. 597–627, Springer Science + Business Media B.V.

Laity, J. E., and N. T. Bridges (2009), Ventifacts on Earth and Mars: Analytical, field, and laboratory studies supporting sand abrasion and windward feature development, *Geomorphology*, *105*, 202–217.

Laity, J. E., and N. T. Bridges (2013), Fundamentals of aeolian sediment transport: Abraded systems, in *Treatise on Geomorphology*, Aeolian Geomorphology, vol. 11, edited by J. Shroder et al., pp. 269–286, Academic Press, San Diego, Calif.

Lancaster, N. (1984), Characteristics and occurrence of wind erosion features in the Namib desert, *Earth Surf. Processes Landforms*, *9*, 469–488.

Langevin, Y., B. Gondet, S. Le Mouélic, O. Gasnault, K. Herkenhoff, D. Blaney, S. Maurice, R. Wiens, and the MSL Science Team (2013), Processing approaches for optimal science exploitation of the ChemCam remote microscopic imager (RMI) during the first 90 days of Curiosity operations, *Lunar Planet. Sci.*, *XLIV*, 1227.

Le Mouélic, S., et al. (2014), The Chemcam remote micro-imager at Gale Crater: Review of the first year on Mars, *Icarus*, doi:10.1016/j.icarus.2014.05.030.

Maki, J., D. Thiessen, A. Pourangi, P. Kobzeff, T. Litwin, L. Scherr, S. Elliott, A. Dingizian, and M. Maimone (2011), The Mars Science Laboratory engineering cameras, *Space Sci. Rev.*, *170*, 77–93, doi:10.1007/s11214-012-9882-4.

Malin, M. C., and K. S. Edgett (2000), Sedimentary rocks of early Mars, *Science*, *290*, 1927–1937, doi:10.1126/science.290.5498.1927.

Malin, M. C., et al. (2010), The Mars Science Laboratory (MSL) Mast-Mounted Cameras (Mastcams) flight instruments, *Lunar Planet. Sci.*, *XLI*, 1123.

Maurice, S., et al. (2012), The ChemCam instrument suite the Mars Science Laboratory (MSL) Rover: Science objectives and Mast Unit Description, *Space Sci. Rev.*, *170*, 95–166, doi:10.1007/s11214-012-9912-2.

Maxson, J. H. (1940), Fluting and faceting of rock fragments, *J. Geol.*, *48*, 717–751.

McCauley, J. F., C. S. Breed, F. El-Baz, M. I. Whitney, M. J. Grolier, and A. W. Ward (1979), Pitted and fluted rocks in the Western Desert of Egypt: Viking comparison, *J. Geophys. Res.*, *84*, 8222–8232, doi:10.1029/JB084iB14p08222.

McKenna-Neumann, C., and R. Gilbert (1986), Aeolian processes and landforms in glaciofluvial environments of southeastern Baffin Island, N.W.T., Canada, in *Aeolian Geomorphology*, edited by W. G. Nickling, pp. 213–235, Allen and Unwin, Boston.

Milliken, R. E., J. P. Grotzinger, and B. J. Thomson (2010), Paleoclimate of Mars as captured by the stratigraphic record of Gale Crater, *Geophys. Res. Lett.*, *37*, L04201, doi:10.1029/2009GL041870.

Ollila, A. M., et al. (2014), Trace element geochemistry (Li, Ba, Sr, and Rb) using *Curiosity*'s ChemCam: Early results for Gale Crater from Bradbury Landing site to Rocknest, *J. Geophys. Res. Planets*, *119*, 255–285, doi:10.1002/2013JE004517.

Palucis, M. C., W. E. Dietrich, A. Hayes, R. M. E. Williams, F. Calef, D. Y. Sumner, S. Gupta, C. Hardgrove, and the MSL Science Team (2013), Origin and evolution of the Peace Vallis fan system that drains into the Curiosity landing area, Gale Crater, *Lunar Planet. Sci.*, *XLIV*, 1607.

Philipps, R. J., et al. (2011), Massive CO_2 deposits sequestered in the south polar layered deposits of Mars, *Science*, *332*, 838–841.

Potter, R. M., and G. R. Rossman (1977), Desert varnish—Importance of clay minerals, *Science*, *196*, 1446–1448.

Potter, R. M., and G. R. Rossman (1979), Mineralogy of manganese dendrites and coatings, *Am. Mineral.*, *64*, 1219–1226.

Richardson, M. I., A. D. Toigo, and C. E. Newman (2007), PlanetWFT: A general purpose, local to global numerical model for planetary atmospheric and climate dynamics, *J. Geophys. Res.*, *112*, E09001, doi:10.1029/2006JE002825.

Rubin, D. M., and R. E. Hunter (1987), Bedform alignment in directionally varying flows, *Science*, *237*, 276–278.

Sharp, R. P. (1949),), Pleistocene ventifacts east of the Big Horn Mountains, Wyoming, *J. Geol.*, *57*, 173–195.

Sharp, R. P. (1964), Wind-driven sand in Coachella Valley, California, *Bull. Geol. Soc. Am.*, *75*, 785–804.

Silvestro, S., L. K. Fenton, D. A. Vaz, N. T. Bridges, and G. G. Ori (2010), Ripple migration and dune activity on Mars: Evidence for dynamic processes, *Geophys. Res. Lett.*, *37*, L20203, doi:10.1029/2010GL044743.

Silvestro, S., D. A. Vaz, R. C. Ewing, A. P. Rossi, L. K. Fenton, T. I. Michaels, J. Flahaut, and P. E. Geissler (2012), Pervasive aeolian activity along rover Curiosity's traverse in Gale Crater, Mars, *Geology*, *41*, 483–486.

Smith, D. E., et al. (2001), Mars Orbiter Laser Altimeter: Experiment summary after the first year of global mapping of Mars, *J. Geophys. Res.*, *106*, 23,689–23,722, doi:10.1029/2000JE001364.

Smith, R. S. U. (1984), Eolian geomorphology of the Devils Playground, Kelso Dunes and Silurian Valley, California, in *Geological Society of America 97th Annual Meeting Field Trip Guidebook, Reno, Nevada*, Western Geological Excursions, vol. 1, edited by J. Lintz, pp. 239–251, Geol. Soc. Am., Boulder, Colo.

Starkey, H. C. (1982), The role of clays in fixing aluminum; contributions to geochemical prospecting for minerals, in *Geological Society of America Bulletin 1278-F*, U.S. Government Printing Office, Washington, D. C. [Available at pubs.usgs.gov/bul/1278f/report.pdf.]

Sullivan, R., et al. (2005), Aeolian processes at the Mars Exploration Rover Meridiani Planum landing site, *Nature*, *436*, 58–61, doi:10.1038/nature03641.

Thiagarajan, N., and C. A. Lee (2004), Trace-element evidence for the origin of desert varnish by direct aqueous atmospheric deposition, *Earth Planet. Sci. Lett.*, *244*, 131–141.

Thomson, B. J., N. T. Bridges, and R. Greeley (2008), Rock abrasion features in the Columbia Hills, Mars, *J. Geophys. Res.*, *113*, E08010, doi:10.1029/2007JE003018.

Thomson, B. J., et al. (2011), Constraints on the origin and evolution of the layered mound in Gale Crater, Mars using Mars Reconnaissance Orbiter data, *Icarus*, *214*, 413–432.

Toigo, A. D., C. Lee, C. E. Newman, and M. I. Richardson (2012), The impact of resolution on the dynamics of the Martian global atmosphere: Varying resolution studies with the MarsWRF GCM, *Icarus*, *221*, 276–288.

Tsoar, H. (2001), Types of aeolian sand dunes and their formation, in *Geomorphological Fluid Mechanics*, edited by N. J. Balmforth and A. Provenzale, pp. 403–429, Springer, Berlin.

Varkonyi, P. L., and J. E. Laity (2012), Formation of surface features on ventifacts: Modeling the role of sand grains rebounding within cavities, *Geomorphology*, *139*, 220–229.

Wiens, R. C., et al. (2012), The ChemCam instrument suite on the Mars Science Laboratory (MSL) Rover: Body unit and combined systems tests, *Space Sci. Rev.*, *170*, 167–227, doi:10.1007/s11214-012-9902-4.

Wilson, P., H. H. Christiansen, and S. M. Ross (2002), The geomorphological context and significance of wind-abraded gravels, boulders and outcrops from the coast of Scotland, *Scott. Geogr. J.*, *118*, 41–45.

Yingst, R. A., et al. (2013), Characteristics of pebble and cobble-sized clasts along the Curiosity rover traverse from Bradbury Landing to Rocknest, *J. Geophys. Res. Planets*, *118*, 2361–2380, doi:10.1002/2013JE004435.